Electron Optical Optimisation of an Imaging Energy Analyser: Real Model Field- and Trajectory Simulations Applied to k-Space Visualisation of Electronic States

Gabriel Armando CEBALLOS, *Krzysztof Piotr GRZELAKOWSKI*

Department of Microelectronics and Nanotechnology, Faculty of Microsystem Electronics and Photonics, Wroclaw University of Science and Technology, ul. Dluga 63, 53-633 Wroclaw, Poland

gabriel.ceballos@pwr.edu.pl, krzysztof.grzelakowski@pwr.edu.pl

DOI: 10.15598/aeee.v19i4.4289

Article history: Received Jul 15, 2021; Revised Sep 21, 2021; Accepted Oct 19, 2021; Published Dec 31, 2021.
This is an open access article under the BY-CC license.

Abstract. *In this report we present a new numerical approach and complex analysis of electron beam propagation based on a realistic model of an optimised imaging spherical deflector analyser. Electron beam trajectory simulations, carried out for real experimental boundaries, enabled us to reveal and explain the unique optical properties which were employed in the instrumental optimisation followed by empirical, spectromicroscopic applications. In terms of numerical treatment, it was possible to verify the low-aberration imaging in reciprocal and real spaces at π and 2π, respectively, and the advantage of energy-selective visualisation of the k-space. Furthermore, this unique feature has been proven and confirmed experimentally by implementing the HeI/HeII monochromatic photon source into our improved spectromicroscopic system and by the energy-selective visualisation of an electronic state projection in the reciprocal plane. A clear correlation between a numerically simulated electronic projection and an experimentally-obtained k-space imaging has been demonstrated.*

Keywords

Aberrations, DEEM, electron microscopy, numerical simulations.

1. Introduction

The research objective of the study is determined by two main aspects regarding the solid state, and material science, as well as a correlated modern multifunctional methodology [1]. The first aspect refers to the growing complexity of modern semiconductor systems accompanied by challenges in new semiconductor devices and detector development which enforces the application of innovative research techniques. In this context the real-time spectromicroscopic observations of the dynamic phenomena related to morphology (real space) and electron band structure (k-space) of complex systems are essential for understanding and optimising of their electronic properties.

In the past a simultaneous application of various surface-sensitive *in situ* techniques were required, preferably integrated into a single instrument. The fast multi-technique surface analysis allows for a detailed, and precise characterisation and description of complex processes in multilayer semiconductor systems [2]. Unfortunately, the migration from one analytical technique to another is intrinsically tied to the loss of the nanometric localisation preselected as the object of analysis. The recovery of this information is often not possible or is at least time consuming, which renders a versatile real-time observation and description of surface processes on the nanometric scale impossible.

Since the dynamic observations must be carried out during the physico-chemical response of the system in real time, widely known scanning methods such as SEM, SAM, AFM, STM, STEM [3], etc. cannot be

considered as potential candidates for time-dependent examination of fast surface processes. The key to solving this problem is the cathode objective lens, in which the sample is a part of the electron optical system. Consequently, the choice of the research tool is reduced to the group of 'parallel imaging' microscopic techniques involving an electrostatic immersion field such as Low Energy Electron Microscopy (LEEM) [4]. The related 'parallel imaging' microscopic technique PEEM (PhotoEmission Electron Microscopy) which only utilises the work function contrast, was originally selected for the dynamic real-time visualisation of chemical reactions on metallic surfaces under external stimuli (Prof. Gerhard Ertl, Nobel Prize in Chemistry 2007) [5].

An ongoing development of comprehensive microscopic surface science methods [1] involves complex electron optical concepts and diverse mechanisms of low energy electron interaction with semiconductor and metallic surfaces. It implies thus the necessity for an advanced theoretical analysis of the electron beam propagation. It results in an essential improvement of imaging aberrations of the novel instrumental solutions which enable different types of contrast: phase (diffraction), chemical (electronic structure), topographic (work function, secondary electrons) and magnetic (polarised electrons), as well as the development of the dedicated analytical imaging technique DEEM (Dual Emission Electron Microscopy) [6].

The proposed methodology utilises these mechanisms based on the original concepts in the field of electron optics, surface physics, electron microscopy and nanotechnology. It is based on the concept of Spherical Deflector Analyser (α-SDA), which exhibits several unique imaging properties regarding optical aberrations, simultaneous k-space and real-image creation (after π and 2π, respectively), synchronous pulse compression in time and space, etc. [7]. However, the first theoretical description of the concept [6] was based on an idealistic model that was neither suitable for real instrumental realisation, and further improvement, nor for optimisation, especially in the context of understanding the experimental results.

Considering these remarks, we have now formulated a complementary analysis of a numerically simulated electron beam propagation as a part of our study, aiming not only at further improvement of the proposed methodology but also, for better understanding of the experimental results in both reciprocal and real space.

2. Real System Representation

2.1. Electron Optical Model

The electron optical model utilises a unique property of position and angle restoration in the case of particle motion in the central force field after a deflection of 2π. It was previously identified, and theoretically described for the first time, based on an idealised field arrangement and simplified assumptions [6]. Therefore, the solutions and implementations related to the 2π deflection concept of innovative imaging system [6] require a more realistic approach, especially regarding the fringing fields and other field perturbations. They should be included into field and trajectory calculations aimed at the optimisation of the energy dispersive properties in the symmetry plane at π. Further deflection by π leads to cancellation of chromatic and geometric aberrations. Such integration of the two independent single π deflections [6], implies the galvanic separation between them and therefore the introduction of an accurate fringing field correction at the coupling positions.

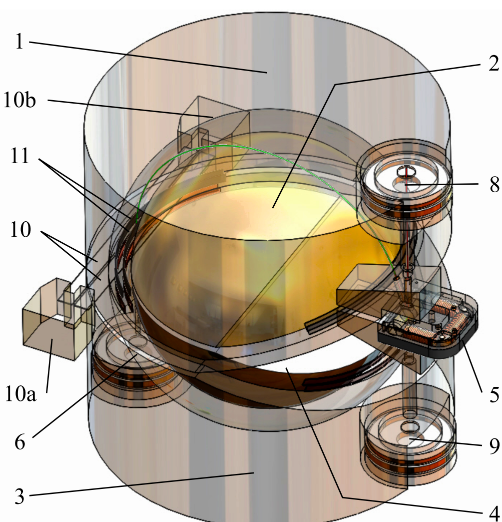

Fig. 1: CAD representation of the spherical analyser model. 1, 2 - first hemispheres; 3, 4 - second hemispheres; 5 - magnetic deflector; 6, 8, 9 - image transfer lenses; 10 - dispersion aperture; 10a, 10b - aperture drivers; 11 - upper correction plates.

Figure 1 illustrates the proposed electron optical model for numerical treatment and its instrumental implementation. The optical optimisation and realisation of this new energy-selective imaging concept required several novel instrumental solutions for a fringing field simulation (11, Fig. 1). The numerical study was initiated by the theoretical confirmation of the correctness of the primary hypothesis and its idealised considerations [6]. A spherical electrode (2, 4, Fig. 1) with positive potential is located at the centre of a slightly larger spherical surface (1, 3, Fig. 1) with negative po-

 © 2021 ADVANCES IN ELECTRICAL AND ELECTRONIC ENGINEERING

tential, causing the formation of a radial electric field in the gap between them, directed to the central symmetry point of the system. An angular field cut-off (15°), which enables the access to this central force field (allowing the input and output of propagating electrons), is reproduced by the 15° magnetic deflector (5, Fig. 1) to restore the primary deflection angle of 2π. As seen in Fig. 1, along the symmetry plane of this system, the spherical electrodes were galvanically divided in two halves, which enabled their independent switching on and off (i.e., one half active – π deflection, two halves active – 2π deflection). The separation also enabled the mechanical implementation of a dispersion aperture (10, Fig. 1) for the energy selection in the gap between them. On the output axis of the first hemisphere, behind the dispersion aperture and the outer electrode, a lens system column (6, Fig. 1) for energy-selective k-space imaging is located (a small opening is made in the outer electrode of the second hemisphere to allow the electrons propagation in this operation mode). On the output axis of the second hemisphere, another lens system column is located (8, Fig. 1). The second column is dedicated to energy-selective real-space imaging (both images: k and r, are brought to the symmetry planes, which are rotated by an angle of $\pi/2$). Switching of only one voltage, namely the second hemisphere, transfers the electron beam from one column to the other and enables quasi-simultaneous imaging of the k- and r-plane at two independent screens. Since electrons trace an 'α' sign during their propagation in the spherical geometry, the system was identified as the α-Spherical Deflector Analyser (α-SDA).

The optical parameters of the system distinguish it from others currently known, also due to the collinear character of such electron propagation before and after penetration of the deflecting field. Both angle and location operator (at the plane after deflection by π) is identical to the operator of a mirror reflection. In a mathematical sense, it means that further propagation of an electron in the alpha-spherical deflector is similar to the propagation of light after reflection in a classical transparent mirror, as it would propagate 'through the looking-glass'. In the idealistic, mathematical approach, this feature makes the α-SDA solution unique: on 'the other side of mirror' all the angles determined by an equation of motion at the input and output are conserved (no geometrical aberrations) and particle energies selective (no chromatic aberrations). According to Fig. 1, we propose now a new realistic model for numerical calculations to simulate the function of the real spectromicroscopic instrument aiming at its further optimisation. Several electron- optical and instrumental improvements were also described, similar to the numerical considerations and presented realistic model. The fringing field correctors (11a, 11b, 11c, 11d - at four electrostatic boundaries and 12 - at two magnetic boundaries) were implemented, according to the practical scheme of Fig. 1.

The numerical conclusions from real-model simulations on the 'dual-imaging' α-SDA system reported below enabled empirical confirmation of the introduced developments and improvements with a better understanding of the experimental results.

2.2. Numerical Treatment

This study uses COMSOL Multiphysics software with its AC/DC module which offers simulation of both electrostatic and magnetic fields along with charged-particle tracing. Preliminary simulations, carried out with the physics-induced settings of mesh and solver, showed the complexity of the problem and the need of an approach consisting of investigating the equilibrium between the results' accuracy and the computational expense required for a valid study evaluation. For this purpose, it was necessary to familiarise ourselves with the underlying mathematics involved in the computation and the control functions offered by the software. It uses the Finite Element Method for the numerical approximation of a physical system and consists of three main fields of preparation: the design of a geometrical, idealistic model with its boundary conditions applied, a mesh that converts it into a discrete set of elements (nodes, boundaries, et cetera), and finally, a solver, which controls the algorithms computing the unknown values over this set [8]. The most challenging aspect of the case under study was the ratio of the measured quantities - aberrations of several µm - to the overall size of the system - for example, the trajectory length of up to half a metre. A minor error in electron deflection at the start would cause a significant displacement at the final screen. This fundamental difficulty was the reason for several adjustments carried out to maintain the local distortions at a sufficiently low level, such that the consequent error does not exceed the measured value. By analysing the preservation of the image geometry at certain image planes of the analyser, we can examine the compliance with this condition as observed from the previous papers [6] and [9].

Among the optimisation measures taken, the most profound one was the simplification of the geometry. We decided to reduce the model body to the space of the non-zero field (both electrostatic and magnetic) and the remaining field-less space which the electrons were to pass through. The elements being the source of the electric field were represented only by their surfaces adjacent to the modelled region. Moreover, a five-centimetre-wide slice parallel to the central trajectory was cut out from the entire spherical analyser model. This simplification was based on the as-

sumption that the influence of the field at a certain distance from the central trajectory can be considered negligible (2.5 times the gap between the hemispheres). Nevertheless, an appropriate boundary at the resulting edges was provided. In the case of the magnetic deflector, its geometry was modelled without any substantial simplifications, to comply with the laws of electromagnetism.

A continuous analytical solution given for any point in the model is an extensive problem to be treated by numerical means. The final solution is obtained instead by solving a linear-equations system derived from Maxwell's fundamental laws of electromagnetism using a set of Hilbert space test functions. These allow for the restriction of a sought local value to be dependent only on several adjacent points of the mesh. As a result, the stiffness matrix, which describes dependencies between all points in the system, becomes sparse [10] and, along with the matrices of unknowns, forms a convenient problem for use with one of the solving algorithms [11]. For this case the Conjugate Gradients method was employed [12]. It takes an average of 23 iterations to minimise the residual error below the specified level from an initial guess, using a non-linear Newton damping method as described in [13]. Here, the imposed termination criterion was the relative solution error, computed as a weighted Euclidean norm, being lower than the level of relative tolerance set to 0.001.

The adaptation of an appropriate mesh to the analytically defined geometrical model has a direct influence on the solution accuracy, since the calculation of the electron trajectory takes the local electrostatic and magnetic field values from a former solution over the set of mesh elements. The denser and uniform the field value discretisation, the better the real trajectory approximation. For the sake of uniformity, a regular quadrilateral element type would be the best solution for this case, but unfortunately, it was found unsuitable. The model body has a complex shape, and certain features interfere with the homogeneity, the correction plates fitted in between the hemispheres or the circular opening in the lower hemisphere, which allows, for example, the transfer of the image to the diffraction imaging column. Therefore, to fit all the boundaries and the interior of the model, a universal non-regular tetrahedral mesh is applied. Several parts have a curved (spherical or, at best, cylindrical) shape, hence the cubic ($k = 3$) shape function order is set to lower the geometrical interpolation error. It enabled providing a more accurate analytical solution by involving as many as 20 nodes belonging to a tetrahedral mesh element in the calculation of the field inside it. In the case of, for example, the linear shape order it would be limited to four nodes only. Yet, the application of a so-defined mesh can cause the occurrence of several inverted curved elements. Thus, an automatic optimisation algorithm is used, to locally lower the shape order to avoid the introduction of a significant error. As a basic assumption for the vicinity of the expected trajectories, a minimum element size of ca. 100 μm has been specified.

A manual iterative re-meshing study conducted, consists of an analysis of the electron acceleration components in each direction along the central trajectory and the minimisation of their differential by inserting several Mesh Control Domains (MCD) to control the computational complexity of the whole problem and yield an acceptable level of inaccuracy of the results at the same time. These domains allowed us to set the assumed low mesh-element size in the regions of local, rapid field-value changes whereas increasing it at a distance from the possible trajectories. The final mesh configuration amounted to over 15.5 million degrees of freedom. Along with the mesh optimisation, to find a threshold over which the error raised to a significant level, the time step for trajectory simulation is adjusted. It has been estimated at about 15 ps, which converted to lateral dimensions, assuming the average electron energy of 1000 eV, equals to 200 μm and correlates with the mesh-element size. The overall time of a complete simulation of the field's distribution and the electron trajectory in most cases reached one hour, most of which the solver spent on the iterative field calculations while the latter electron tracing typically took several minutes.

2.3. Magnetic- and Electrostatic Field Optimisation

As indicated in the real system model in Fig. 1, its complex field configuration is implied by the necessity for recovery of the field fraction that is lost because of the angular '15-degree-cut-off' in the spherical electrostatic field. This perturbation of the perfect central force field is practically unavoidable since the ideal spherical field considered previously is internally 'closed' for charged particle penetration. Therefore, to restore the full angle deflection of 2π, i.e., the mentioned 'α-like' quasi-linear electron beam propagation (Fig. 1), the same deflection of 15° was assured by the instrumental implementation of the magnetic sector field (5, Fig. 1). An additional advantage arises from the well-known property that the deflection angle of a magnetic field is inversely transformed when the direction of propagation changes. Since the electrons pass through the magnetic sector field twice, the mirror symmetry of the system brings the electron beam at the output to the same primary direction at the system entrance.

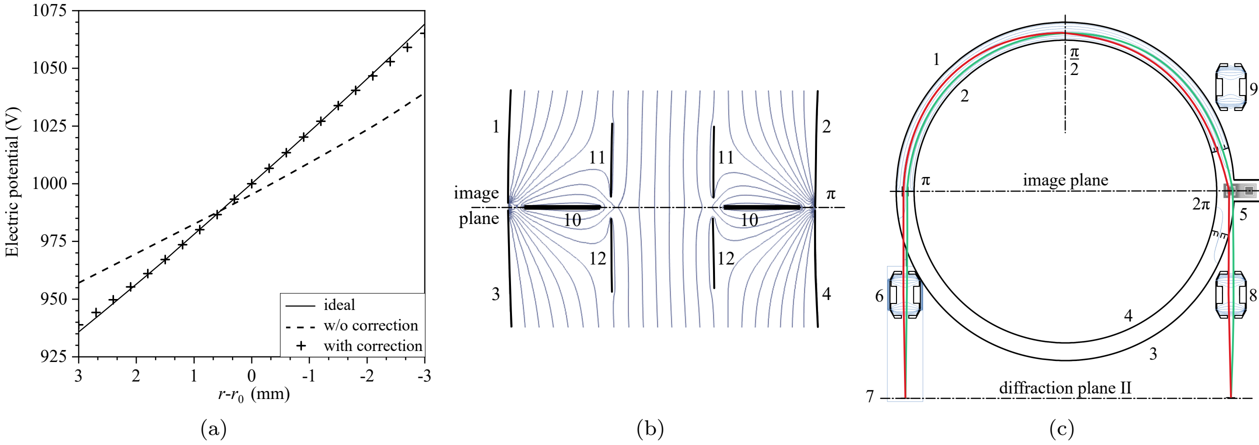

Fig. 2: (a), (b) Fringing field correction after π deflection, and (c) cross-section of the system model geometry with exemplary trajectory. Element numeration as in Fig. 1, additionally: 7 - diffraction plane; 12 - lower correction plates.

However, the intended doubling of the beam travel through the magnetic deflector means a fourfold contribution of the field boundaries, making the problem more significant. Additionally, as already mentioned in the previous section, the spherical electrodes must be galvanically separated into two halves enabling their independent switching on and off (i.e., one-half active – π deflection, two halves active – 2π deflection, Fig. 2(a). Also, the mechanical implementation (in the gap between them) of the dispersion aperture (10, Fig. 1) for energy selection required a discernible distance between the spheres. As a consequence, two further field boundaries occur in the system. Thus, this elegant conceptual solution in the idealistic approach enforces some electron-optical compromise when brought into an instrumental realisation: the described distortion of the ideal spherical system implements in total six fringing field regions (four electrostatic at the entrance and exit, and two magnetic on both sides of the sector field) which, because of the compact instrument size, contribute to the electron-optical picture and cannot be neglected.

In this study, we have created a realistic model in which we consider the real contribution of all existing field boundaries. In the earlier intuitive model, a perfect radial field distribution at the 'cut-offs' was assumed in the simplified model to carry out the analytical, rough description. Figure 2(a) illustrates the radial electrostatic potential distribution just at the capacitor boundary in three considered cases: a theoretical curve of the ideal spherical system (solid line), potential distribution with (dashed line) and without field correction (cross marks). The advantage of the last solution is obvious: the potential distribution (cross marks) with a system of rings at the electrode terminations follows the ideal curve (solid line) nearly perfectly. Therefore, during instrumental realisation, the system was enhanced by external field correctors and then by electron optical trajectory simulations considering the correcting rings arrangement and its field distribution (3, Fig. 2(a)) as a contribution to the correct description of spectromicroscopic imaging. Finally, Fig. 2(b) indicates potential restoration even if the upper and lower hemispheres are galvanically separated.

Exploiting the new potential configuration from Fig. 2(a), we could now 'calibrate' the system to meet the physical, experimental conditions and to correlate the numerical simulations with the first experimental results. Thus, we have adjusted the initial conditions for the π deflection first in the diffraction mode, i.e., the second hemisphere was switched off.

Prior to the analyser potential's calibration, the transfer lenses' focal length and the sector field value were optimised. The lens was simulated separately and the resulting focusing potential value was transferred to the main system model. Then a test condition was arranged by releasing a single electron from the reciprocal plane (7, Fig. 2(c)) at a right angle towards the magnetic deflector centre. The proper sector field value was sought to align the trajectory onto the tangent at the first hemisphere boundary. Having this initial configuration, we were able to calibrate the next stages of the instrument operation.

The described electrostatic deflection system allows the introduction of correction parameters at several points along the electron path to superpose with the originally defined idealistic potential values. First, the electron energy value in the central force-field equation was slightly changed in order to modify the deflection conditions in the first hemisphere and correct the trajectory radius after π deflection. Then, another coefficient was introduced on the correction rings (11, Fig. 2(b)) intended to combine with their calculated ideal potentials (dependent on the imaging mode LEEM/LEED) in order to fix a right angle at this

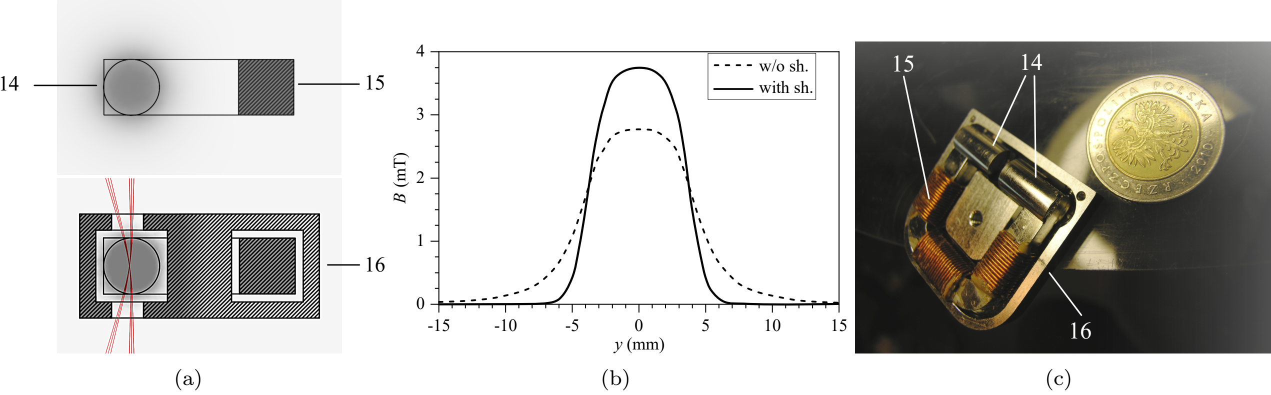

Fig. 3: (a) Magnetic field distribution without (upper) and with (lower) magnetic shielding applied. (b) Comparison of the field strength along the vertical axis in the two cases. (c) View of a partly assembled deflector. 14 - pole pieces, 15 - magnetic core with coils wound, 16 - magnetic shielding case.

boundary so that the electron hits the centre of the screen (7, Fig. 2(c)). Next, the lower hemisphere was turned on and the deflection potentials were shifted again by a small delta to align the trajectory to the ideal radius after the $2\pi - 15°$ (345°) deflection. Lastly, another symmetrical change was applied to the values of the correction rings' potentials at this boundary to adjust the outbound angle to match the inbound one (15°), as it is mandatory to comply with the sector field symmetry requirements. After this complex numerical adjustment procedure (to satisfy geometrical boundary conditions), the theoretical model system demonstrated in Fig. 2(c) was utilised further in the simulation of electron beam propagation for diverse constructional versions and improvements described in the next section. As mentioned previously, the abrupt termination of the spherical electrostatic field at the sphere edges introduces significant perturbation (dashed line in Fig. 2(a)) in the ideal field distribution (represented by a solid line in Fig. 2(a)). Since the relative contribution of this perturbation is inversely proportional to the radius of the system (in our case, 60 mm only to fit 8" CF-flange), we considered diverse constructional solutions for fringing field corrections and found that the installation of two spherical rings restores the ideal field shape at the edges (Fig. 2(b)). In effect, the radial potential distribution at the termination plane (crosses in Fig. 2(a)) nearly perfectly follows (especially within the electron beam) the ideal spherical potential curve (solid line in Fig. 2(a)).

The same problem of fringing fields occurred in the case of the magnetic sector field at pole piece edges (upper part of Fig. 3(a) and corresponding distribution curve - dashed line in Fig. 3(b). The calculated fringing fields result in the smearing and widening of the magnetic deflection and further affect the imaging property significantly and adversely. Therefore, we considered an additional external magnetic element with high permeability resulting in the sharpening of the field (solid line in Fig. 3(b)). As our field simulations demonstrate, the change in deflection angle will be reduced close to the central point as shown in Fig. 3(b), which significantly minimises tangential aberrations [14].

2.4. Instrumental Improvement

The issue of the fringing field, numerically identified in the case of imaging analyser in the previous section, confirmed the necessity for instrumental improvement. The instrumental solutions introduced for electrostatic and magnetic fringing-fields compensation can be identified respectively in the picture of the partially disassembled imaging analyser (Fig. 8) and magnetic sector field image (Fig. 3(c)). A set of six round strip electrodes (11 and 13, Fig. 8) is placed in the gap between spherical electrodes in the upper and in the lower part of the imaging analyser and their potentials are set to the value of the idealistic model (solid line in Fig. 2(a)). The simulated central force field at the edges is terminated by means of a plain shielding electrode with a small central opening that limits the smearing effect of the electrostatic field at the system boundaries. The same function is realised by the additional magnetic shielding element in the case of electromagnetic deflector shown in Fig. 3(c). With an exception of small input/output openings, it is realised as a perfectly closed toroidal Permenorm [15] box, which is magnetically and electrically isolated from the deflector by means of sapphire balls. To restore its unique magnetic properties after fabrication, it was carefully annealed in a vacuum oven.

3. Real System Aberrations

3.1. Geometrical Aberrations

As mentioned in the introduction, the original theoretical description of the spherical imaging analyser concept was based on an idealistic model. In this section, our detailed theoretical and numerical analysis aims not only at further improvements but also a better understanding of the obtained experimental results in both reciprocal and real space. We start with the aspect of geometrical aberrations at the main imaging planes of the modified system according to the results of the previous section: at the symmetry plane after π and 2π deflection as well as after $\pi/2$ for the reciprocal plane. A numerical point object was determined by a set of eight electron trajectories which form a pencil of rays, with angles ranging from 0° to 1°, as expected in the real experiment. Considering the magnification, these values refer to the actual range of about 50° at the sample. The electrons' energies were fixed at a single value (no smearing assumed), related to the Fermi level of the sample, to separate the regarded sort of aberrations from other types. Thus, the only factors of the measured aberrations were the electron starting positions and angles.

Initial simulation results are shown in Fig. 4(a) and Fig. 4(b). To visualise the level of contribution of a certain initial angle to the image aberration, the point size was correlated to an expected intensity level estimated by a cosine-squared distribution. One can observe that the aberrations induced by the π deflection exhibit a vertical symmetry only. This is due to the deflecting characteristics of the central force field, which cause any displacement in the direction of the field gradient to have a negative value after π deflection, which explains the occurrence of same-size points in pairs on the right-hand side of the graph. Nonetheless, this phenomenon meets its compensation after 2π deflection, where the initial image symmetry is restored with a slight distortion for the highest angle values, which is presented in Fig. 4(b). The X and Y scales were normalised, in order to estimate the possible result of stigmatisation and thereby emphasise the aberration-corrected geometry of the image in the real system. We decided to simulate a narrower range of pencil angles (0° to 0.15°), as we expected them to exhibit less aberration after 2π deflection. This assumption was confirmed by the results shown in Fig. 4(c). The upper part of the plot shows the image as simulated, but below a more emphatic image is provided as the estimated result of a possible later stigmatisation adjustment.

The stigmatised image in Fig. 4(b) exhibits a spherical aberration level of about 30–40 µm of a total blur of a single real image point, which is related to the corresponding value from Fig. 4(a), i.e., 80–100 µm, indicates at least a twofold decrease of aberrations in the second hemisphere deflection, which is even lower for small initial angles: 3–4 µm (Fig. 4(c)). It allows us to conclude the potential real image resolution to be below 100 nm, considering the 40–50× magnification of the image related to the sample surface.

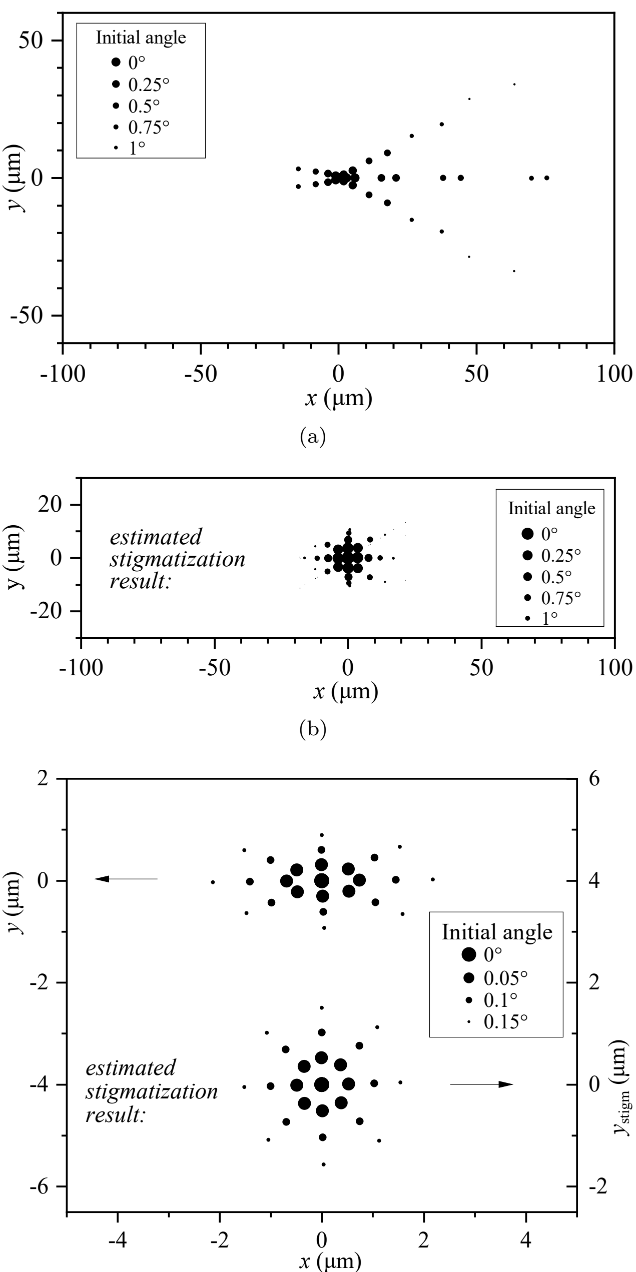

Fig. 4: (a) Spherical aberrations after π deflection for high initial angle range (0° to 1°). (b) Spherical aberrations after 2π deflection. Vertical scale adjusted to show the possible stigmatisation result. (c) Spherical aberrations after 2π deflection for low initial angle. The upper image shows the image as-simulated, below - the same image re-scaled to demonstrate the possible stigmatisation result.

3.2. Chromatic Aberrations

Chromatic aberrations must be considered when an energy distribution caused by the photoemission mechanism is evoked by high-energy photons, as in the case of our experiment. Since the primary energy of applied illumination from the helium plasma discharge reaches 21 eV, we assume in our numerical treatment the energy variation in the range of several electron-volts (related to the object's Fermi level). Figure 5 illustrates the effect of electron beam interaction with the combined magnetic and electrostatic central force field and its behaviour after π and 2π deflection. We have found that the highest energy dispersion in the case of a combined magnetic and electrostatic spherical field occurs just in the symmetry plane after π, which determines the optimal location for dispersion aperture. As indicated in Fig. 2(c) and Fig. 8, it was introduced in the narrow gap between field simulating rings described in Subsec. 2.3. Thus, Fig. 5 illustrates the impact of chromatic aberrations of the 'real' modified imaging analyser on the quality of the final image: after π deflection (maximal dispersion) and after 2π deflection (where dispersion is fully compensated). In other words, the modified, 'real' spherical imaging analyser preserves one of the unique optical properties attributed to an ideal central force field, namely achromatic behaviour after 2π deflection (horizontal curve in Fig. 5(a)). Near the central orbit, the electron trajectory shift versus energy exhibits a linear character. Introducing all the real system parameters into calculations as discussed in the previous sections, we have determined the resolving power of the energy analyser as ~ 5 meV·µm^{-1}. Thus, in the real experiment that we have carried out with HeI (21.4 eV) and ~ 50 µm dispersion aperture, we were able to obtain an energy resolution of around ± 100 meV after π deflection. However, the lateral resolution at this stage corresponds to the size of the aperture making imaging impossible. We, therefore, employ a second, 'mirrored' π deflection that compensates for the dispersion of the first one and radically raises the resolving power, as indicated by the horizontal dependence shown in Fig. 5(a). Therefore, all electron trajectories that spread after π are brought into a point after 2π as indicated by arrows in Fig. 5(b). The electron-optical compensation is also utilised in the case of k-space (diffraction plane) that occurs after $\pi/2$ deflection (Fig. 2(c)) in another symmetry plane of the system and will be discussed in the next section.

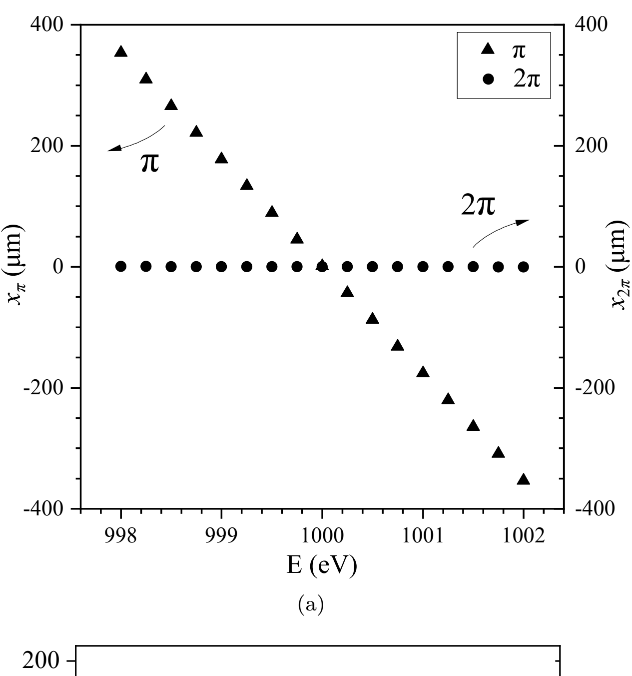

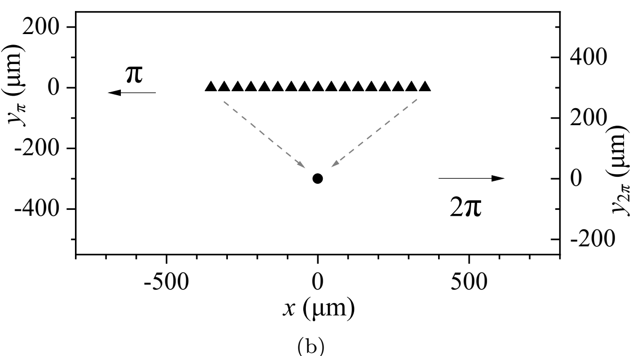

Fig. 5: Comparison of chromatic aberrations after π and 2π deflection, shown (a) as one-directional displacement related to the initial energy and (b) as two-dimensional displacement to scale (image shrunk to literally one point after 2π).

4. k-Space Visualisation

4.1. Modelling of Electronic Structures

In this section, several different electronic structures considering energy, position and emission angle were considered aiming at a better understanding of energy-selective k-space imaging. Three features were modelled to appear in a reciprocal plane after $\pi/2$ deflection (Fig. 6(a)): a vertical one at 1 eV below the Fermi level (999 eV 'system' energy), a horizontal one at 1 eV above and one circular feature just at the Fermi level. When classically projected at the screen (without an imaging energy analyser), many single features overlap in the image and can't be distinguished as seen in Fig. 6(a). A further ('mirrored') deflection by $\pi/2$ that corresponds to the Fourier transform, converts

the angles and energies into positions (distances from the central point) in the real image symmetry plane, where the dispersion aperture operates and therefore the energy selection takes place.

As seen in Fig. 6(b), electronic structures are reduced to three concentrated groups of electron trajectories distinguished by energy alone. Although in this plane no single k-space feature attributed to the same electronic structure can be imaged correctly, it is the optimal position to select this feature. To project the electronic structure, modelled as an object of imaging in diffraction plane I (Fig. 6(a)) at the screen (diffraction plane II, Fig. 2(c)), the transfer lens '6' in Fig. 2(c) must be activated, forming the image shown in Fig. 6(c). Disregarding a slight demagnification, this image is just the simultaneous reproduction of the three structures modelled in Fig. 6(a). Because in this simulation we have fully opened the dispersion aperture numerically (all features are passing through), as illustrated in Fig. 6(b). It reproduces just the situation, when the imaging energy analysis is not involved. The following section presents the advantages of energy-selective imaging.

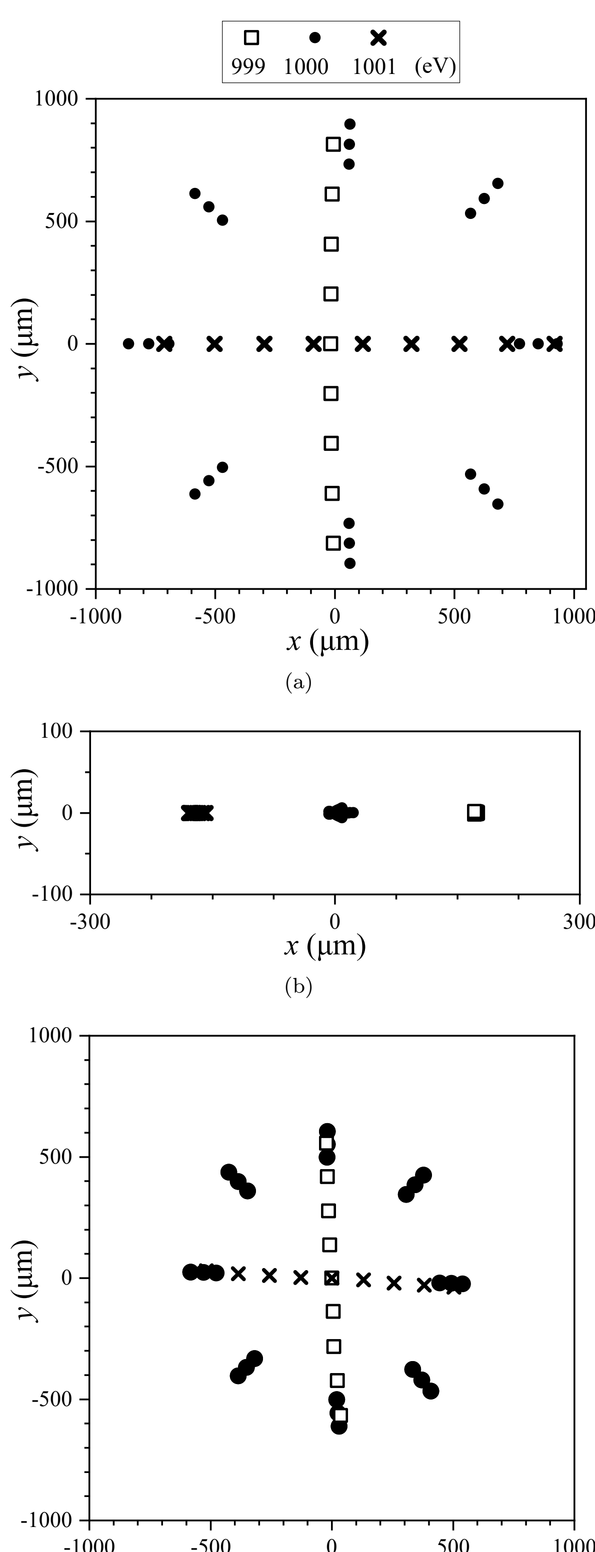

Fig. 6: Visualisation of three features (marked by crosses, solid dots and squares) of an artificial electronic structure of energies near the Fermi level, imaged (a) in diffraction plane I (after $\pi/2$ defl.), (b) in image plane (after π defl.) and (c) in diffraction plane II.

4.2. Effect of Energy-Selective Imaging

The mechanism of energy-selective projection of the electronic structure in k-space is schematically shown in Fig. 7(a) for three aperture locations (Fig. 7(b), Fig. 7(c) and Fig. 7(d). Contrary to the situation from Fig. 6(b), the sufficiently slim and properly adjusted, appropriately positioned dispersion aperture enables the selection of individual information from the k-space related to different electronic features. Figure 7 demonstrates the beneficial change in the final image when the real dispersion aperture is simulated in numerical calculations. Its width was numerically set to the realistic value of 100 µm that corresponds to an energy window of ± 250 meV, sufficiently low to differentiate one feature from another.

The result of energy selection at 1 eV above the Fermi level (which corresponds to the system pass energy equal to 1001 eV), shown in Fig. 7(b) ('vertical' feature) as the virtual aperture is numerically brought to position (b). Since all other electrons are blocked by the aperture, the referred features, i.e., 'horizontal' and 'circular' (Fig. 6(c)) are also suppressed in the final image. Analogically, when the aperture slit is shifted to the central position correlated to the energy of Fermi level ('circular' feature from Fig. 6(c)), the appearance of the other two aspects below and above the Fermi level is blocked, in the process of the energy-selective projection, and only one, namely 'circular' feature manifests itself in

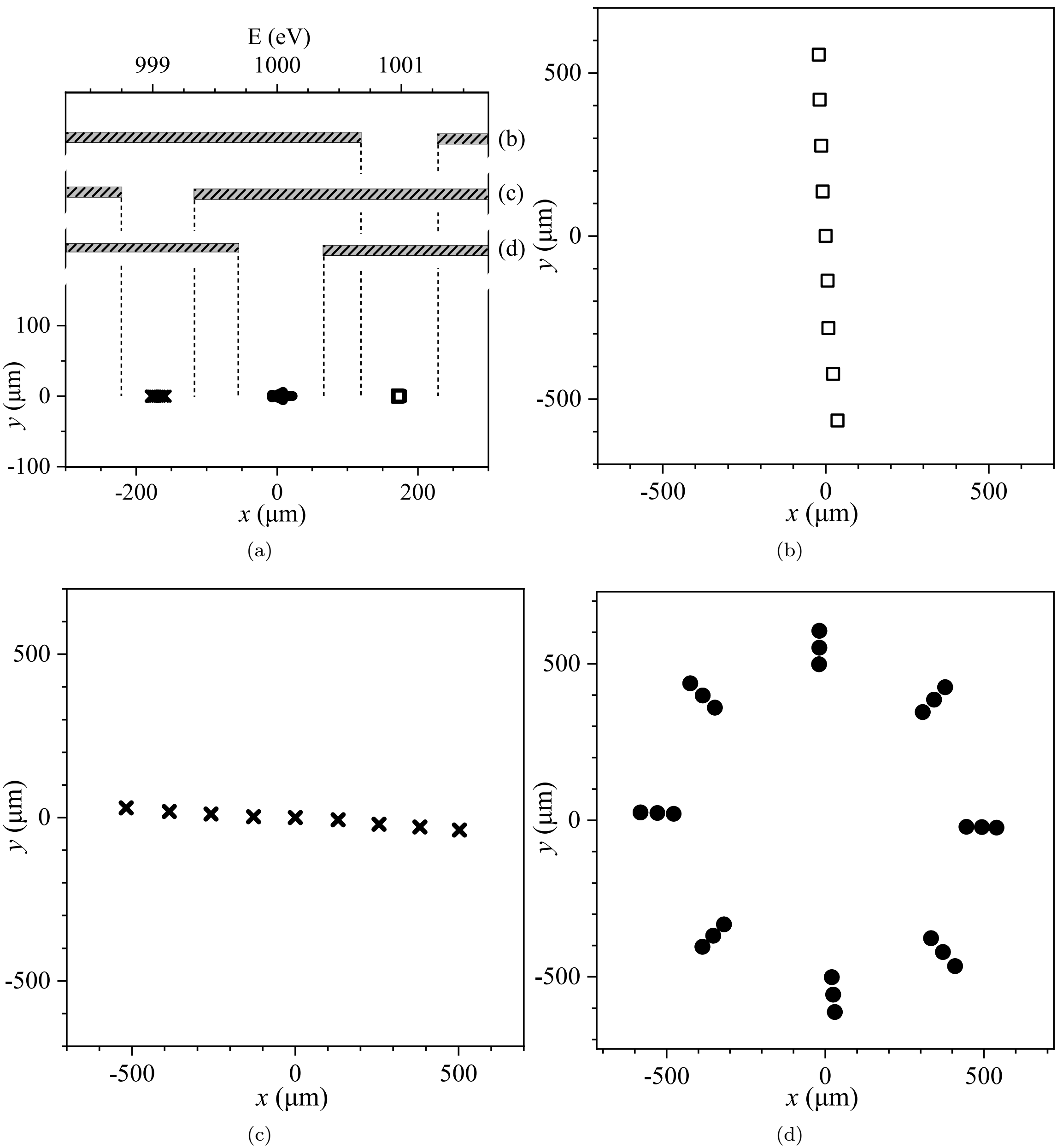

Fig. 7: Simulation results of the energy-selective imaging: (a) position of the dispersive aperture in the image plane and ((b), (c), (d)) images of consecutive filtered features at the diffraction plane II.

the image, as indicated in Fig. 7(d). The same is valid for the energy-selective visualisation of the third modelled feature 1 eV below Fermi level at aperture position "c" (Fig. 7(c)).

Numerical calculations and simulations based on the presented real model demonstrate the unique capabilities of the proposed methodology and evidenced several important aspects of an instrumental realisation and its improvement, especially regarding electrostatic field boundaries and the optimisation of the magnetic sector field. The following section presents the instrumental realisation related to the analysed electron optical subjects.

5. Instrumental Realisation

5.1. Imaging Energy Analyser

The novel imaging UPS facility shown in Fig. 9 is the result of an instrumental unification of two advanced systems: monochromatic VUV HeI/II light source [16] and DEEM spectromicroscope. To optimise this complex methodology, we focused our interest on the accurate description of the instrumental and experimental realisation, especially in the main electron optical unit, namely the imaging spherical analyser illustrated in the final form in Fig. 8.

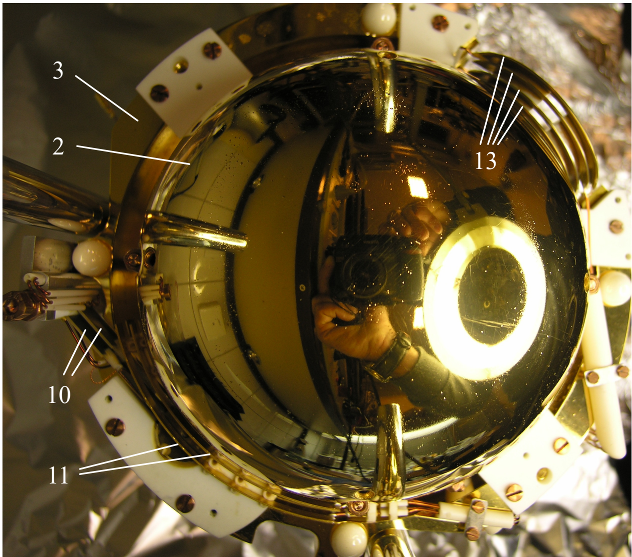

Fig. 8: The view of a partly assembled α-SDA (element numbering as in Fig. 1 and Fig. 2).

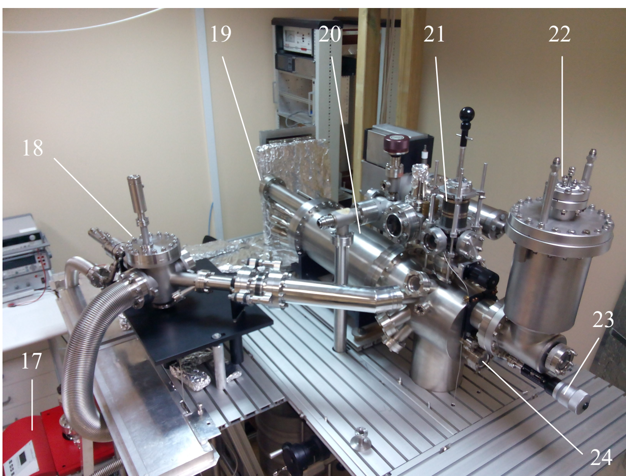

Fig. 9: A photograph of the DEEM system in our laboratory. 17 - HeI/HeII lamp pumping system, 18 - HeI/HeII lamp, 19 - diffraction image screen, 20 - DEEM main vacuum chamber, 21 - probe exchange system, 22 - Ti sublimation pump, 23 - external part of electron beam sample illumination system, 24 - real image screen.

It is a central, electron-optical as well constructional part of a whole system (20, Fig. 9) and fully consistent with the realistic, numerical model described in the previous sections as revealed in Fig. 8.

A realistic 3D model considered first as a numerical object for electron trajectory calculations carried out in this study accurately replicates the same geometry as in the instrumental realisation (Fig. 8). As in the optical simulations and numerical treatment (discussed in Subsec. 2.3.), the primary spherical electrodes are equipped with a system of field simulating rings at their boundaries which reproduces the same 'ideal' radial field as generated inside the spheres. Figure 8 shows the top view of the imaging analyser interior after removing the upper spherical external electrode. Two kinds of ring electrode systems are used at the field simulation at the gap between upper and lower sphere: four element arrangement (13, Fig. 8) at the beam inlet/outlet (since the e-beam passes twice after 2π deflection) and two element arrangements (after π deflection). The same instrumental solution is applied to the 'hidden' (not visible in Fig. 8) lower sphere - between them a cylindrical shield (11, Fig. 8) of the dispersion aperture is introduced. The dashed line indicates the main electron optical trajectory.

5.2. Final Appearance of the UPS/DEEM System

The complete experimental system illustrated in Fig. 9 was assembled according to the description presented in the previous sections. It consists of two main components: VUV HeI/HeII monochromatic illumination source [16] (18, left hand side in Fig. 9) and imaging spectromicroscope DEEM (20, right hand side in Fig. 9). A novel primary electron beam system '24' for the low energy electron diffraction and imaging (partially visible in Fig. 9) is internally attached to the microscope column. As seen in Fig. 9, the VUV HeI/HeII photon source is mounted on a large aluminium plate that can be adjusted (by means of five manipulations: two tilts, X/Y shift and Z-motion) to assure a perfect fine positioning of the $\sim$ 500 μm photon beam at the electron optical sample centre. The first two components are pumped by three dedicated pumping systems: the VUV HeI/HeII source and monochromator separately by two independent high vacuum systems (17, Fig. 9) and the spectromicroscope itself by a three-stage (mechanical, turbo and ion pump) UHV system. Since the electron beam illumination system is directly attached to the spectromicroscope body, it automatically becomes a part of its vacuum system. As illustrated in Fig. 9 it is additionally equipped with a liquid nitrogen Ti-sputtering unit (22), which assures a better vacuum and higher pumping speed during the time of experiments. On the top of the horizontally mounted microscope chamber, a small sample preparation system (21) has been attached with its dedicated ion pump. It allows not only the sample thermal treatment and in situ modifications but also its fast exchange using a wobble-stick (Fig. 9). Additionally, a vacuum separating plate valve has been fitted to prevent the system venting during the process.

6. Experimental Proof

The assembled experimental facility illustrated in Fig. 9 was first used for the imaging UPS experiment for the (110) single face of molybdenum crystal and

tuned according to our numerical simulations to visualise the valence band structure in the vicinity of Fermi level. The VUV system has been activated at HeI line to illuminate the molybdenum surface with sufficient energy (21.4 eV) to excite electrons from the valence band. The pass energy of the imaging spherical analyser has been tuned for selective detection and imaging of the angular structure that occurs at the diffraction plane.

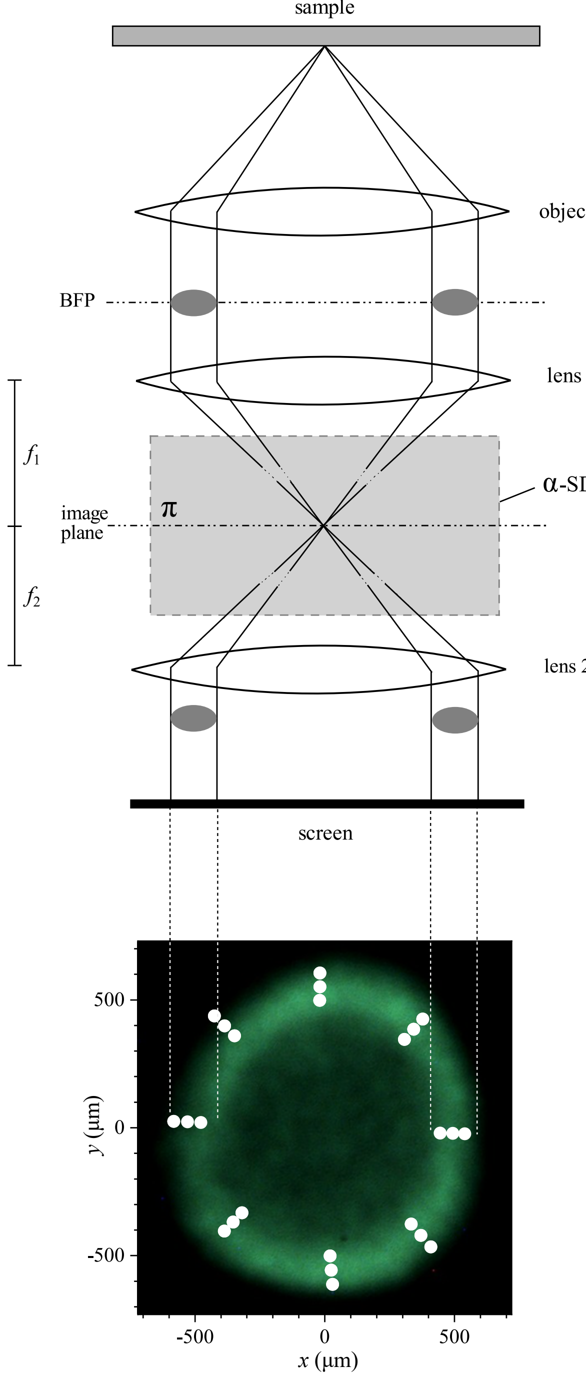

Fig. 10: Simplified electron optical diagram of the imaging of the k-space feature observed in the experiment and DEEM image with the feature simulation plot from Fig. 7(d) overlaid.

Based on our numerical image simulations executed in Subsec. 2.3. we were able to retrace the experimental 2D structure of the valence band electrons towards the emission area at the crystal surface. In the upper part of Fig. 10, the adequate electron beam traces are schematically indicated to correlate the experimental k-space projection with its electron optical relation to the 2D structure in the system diffraction plane BFP. Since the 2D Fermi level is not affected by the crystallography of (110) molybdenum single face, it is consistent with the anisotropic behaviour of the photoemission simulated in our numerical treatment (Subsec. 2.3.), reflected by dots in the lower part of Fig. 10.

7. Conclusions

In this paper an innovative methodology for electronic structure probing with DEEM spectromicroscope was analysed and presented. Since the previous theoretical descriptions of the concept were based on a purely idealistic model (that only partially relates to the real system), in this study we carried out a series of numerical simulations that reveal the empirical conditions as closely as possible. It results not only in better understanding and description of proposed and realised experiments but also allows the further improvement of the spectromicroscopic system.

The worsening of the imaging conditions of the analyser due to the electric and magnetic fringing field has been studied and the consequent instrumental improvements were reported. The extremely low geometrical and chromatic aberrations of the imaging spherical analyser, implied by their intended compensation (governed by the mirror symmetry of the system) were demonstrated on the basis of numerical simulations and described in this study. Finally, real experimental boundaries were applied to the created numerical model and correlated to the experimental k-space image.

The compliance obtained confirms that the developed numerical model of the real system reveals very well its assumed empirical advantages and properties and can be used for the further electron optical improvements regarding the methodology of energy selective band structure visualisation.

Acknowledgment

We would like to thank Prof. Marek Tlaczala for the fruitful discussions and motivation for this study. Our acknowledgements are also due to Dr. Beata Sciana, Dr. Damian Radziewicz and Dr. Wojciech Dawidowski

for their constant help and participation in preparing the experiment. We also thank Janusz Krajniak for his contribution to electronics and software.

This research was supported and fully financed by National Science Centre, Grant no. 2015/17/B/ST7/03815.

This work was co-financed by the Wroclaw University of Science and Technology K70W12D02 subsidy. This work was accomplished thanks to the product indicators and result indicators achieved within the projects co-financed by the European Union within the European Regional Development Fund, through a grant from the Innovative Economy (POIG.01.01.02-00-008/08-05).

Author Contributions

K.P.G. set the aim of this research and provided theoretical and technical data for the simulations. G.A.C. designed and optimised the numerical model, conducted the simulations, and evaluated their results. G.A.C. and K.P.G. experimented on the DEEM system. Both authors contributed to the analysis of obtained findings and both drafted, edited, and revised the paper.

References

[1] BAUER, E. *Surface Microscopy with Low Energy Electrons*. 1st ed. New York: Springer Science+Business, 2014. ISBN 978-1-4939-0934-6.

[2] RIDLEY, B. K. *Electrons and Phonons in Semiconductor Multilayers*. 2nd ed. Cambridge: Cambridge University Press, 2014. ISBN 978-1-107-42457-9.

[3] CZANDERNA, A. W. *Methods of Surface Analysis*. 1st ed. New York: Elsevier Science, 2012. ISBN 978-0-444-59645-1.

[4] TELIEPS, W. and E. BAUER. An analytical reflection and emission UHV surface electron microscope. *Ultramicroscopy*. 1985, vol. 17, iss. 1, pp. 57–65. ISSN 1879-2723. DOI: 10.1016/0304-3991(85)90177-9.

[5] ERTL, G. Reactions at Surfaces: From Atoms to Complexity (Nobel Lecture). *Angewandte Chemie International Edition*. 2008, vol. 47, iss. 19, pp. 3524–3535. ISSN 1521-3773. DOI: 10.1002/anie.200800480.

[6] GRZELAKOWSKI, K. P. A flange on electron spectromicroscope with spherical deflector analyzer—simultaneous imaging of reciprocal and real spaces. *Ultramicroscopy*. 2013, vol. 130, iss. 1, pp. 29–35. ISSN 1879-2723. DOI: 10.1016/j.ultramic.2013.02.015.

[7] GRZELAKOWSKI, K. P. and R. M. TROMP. Temporal and lateral electron pulse compression by a compact spherical electrostatic capacitor. *Ultramicroscopy*. 2013, vol. 130, iss. 1, pp. 36–43. ISSN 1879-2723. DOI: 10.1016/j.ultramic.2013.03.022.

[8] COMSOL. *Comsol Multiphysics Reference Manual*. [Online]. Version 5.4. Burlington, 2018. Available at: https://doc.comsol.com/5.4/doc/com.comsol.help.comsol/COMSOL_ReferenceManual.pdf.

[9] GRZELAKOWSKI, K. P. A novel imaging energy filter for cathode lens electron microscopy. *Ultramicroscopy*. 2012, vol. 116, iss. 1, pp. 95–105. ISSN 1879-2723. DOI: 10.1016/j.ultramic.2012.03.010.

[10] SAAD, Y. *Iterative Methods for Sparse Linear Systems*. 2nd ed. Philadelphia: Society for Industrial and Applied Mathematics, 2003. ISBN 978-0-89871-534-7.

[11] AMESTOY, P. R., I. S. DUFF, J.-Y. L'EXCELLENT and J. KOSTER. A Fully Asynchronous Multifrontal Solver Using Distributed Dynamic Scheduling. *SIAM Journal on Matrix Analysis and Applications*. 2001, vol. 23, iss. 1, pp. 15–41. ISSN 1095-7162. DOI: 10.1137/S0895479899358194.

[12] HESTENES, M. R. and E. STIEFEL. Methods of Conjugate Gradients for Solving Linear Systems. *Journal of Research of the National Bureau of Standards*. 1952, vol. 49, iss. 6, pp. 409–436. ISSN 2165-7254. DOI: 10.6028/jres.049.044.

[13] DEUFLHARD, P. A modified Newton method for the solution of ill-conditioned systems of nonlinear equations with application to multiple shooting. *Numerische Mathematik*. 1974, vol. 22, iss. 4, pp. 289–315. ISSN 0945-3245. DOI: 10.1007/BF01406969.

[14] GLASER, W. *Grundlagen der Elektronenoptik*. Vienna: Springer-Verlag, 1952. ISBN 978-3-662-23620-8.

[15] VACUUMSCHMELZE GmbH. *Soft Magnetic Materials and Semi-finished Products*. [Online]. Hanau, 2002. Available at: https://vacuumschmelze.com/03_Documents/Brochures/PHT%20001%20en.pdf.

[16] FOCUS GmbH. *HIS 14 HD Mono: monochromatized VUV source*. [Online]. Hunstetten, 2020. Available at: https://www.focus-gmbh.com/wp-content/uploads/2020/03/HIS14HDMono_Flyer_2016_v6_klein.pdf.

About Authors

Gabriel Armando CEBALLOS was born in Lodz, Poland. He received his M.Sc. in Mechatronics from Wroclaw University of Science and Technology in 2017. His current research is tied to the development of the DEEM system.

Krzysztof Piotr GRZELAKOWSKI (corresponding author) was born in Wroclaw, Poland. He received his M.Sc. in Physics from the University of Wroclaw in 1985 and Ph.D. from the Technical University of Clausthal, Germany in 1994. His research interests include surface science, electron optics, electron microscopy.